Variation of loads on a three-bladed horizontal axis tidal turbine with frequency and blade position

Grégory S. Payne[a,*], Tim Stallard[b], Rodrigo Martinez[c], Tom Bruce[c]

[a]*Department of Naval Architecture, Ocean & Marine Engineering, University of Strathclyde, Glasgow G4 0LZ, UK*
[b]*School of Mechanical, Aerospace and Civil Engineering, University of Manchester, Manchester M13 9PL, UK*
[c]*Institute for Energy Systems, School of Engineering, University of Edinburgh, King's Buildings, Mayfield Road Edinburgh EH9 3FB, UK*

Abstract

Sustainable and cost effective design for tidal current turbines requires knowledge of the complex nature of unsteady loads on turbine components including blades, rotor and support structure. This study investigates experimentally the variation with frequency of rotor thrust and torque loads, of streamwise root bending moment on individual blades and of loads on foundation at the bed. Comparisons between these different load spectra are also established. The impact of absolute rotor angular position on blade and rotor thrust loads is also examined. The study is based on measurements from a 1/15 scale, three-bladed, horizontal axis machine tested in a recirculating flume, in onset flows of 3% and 12% turbulence intensity. It is found that for frequencies below the rotational frequency, load spectra are correlated to spectral density of the onset flow velocity. Above the rotational frequency, loads are mainly affected by turbine operation phenomena. The

*Corresponding author
Email address: gregory.payne@strath.ac.uk (Grégory S. Payne)

tower shadowing effect is clearly identified through frequency and angular analysis. Finally, thrust loads as experienced by the rotor alone are for the first time compared with streamwise and transverse foundation loads. Higher frequency loads experienced by the tower are shown to be affected by different vortex shedding regimes associated with different regions of the wake. All the experimental measurements presented in this article can be accessed from http://dx.doi.org/10.7488/ds/2338 .
Keywords: tidal turbine, frequency analysis, loads, physical experiment

1. Introduction

Systems for generation of electricity from tidal streams have attracted increasing interest in recent decades. Although a variety of design concepts have been developed, the most widely studied systems are horizontal axis turbines, similar in configuration to wind turbines. Several developers have now deployed such turbines at full-scale test sites (Parkinson and Collier, 2016; MayGen Ltd., 2016). However, there remain challenges for design, particularly with regard to accurate prediction of the unsteady loads that determine component specification for adequate operational life. For the similar case of a wind turbine, unsteady loading on blades, and hence on the turbine, is due to the rotation of the blades through a non-uniform onset flow and in proximity to a fixed support structure. Onset turbulence also play a role in the unsteady loading. The influence of these factors on wind turbine design have received attention through experimental studies such as the MEXICO campaign (Schepers et al., 2014) and CFD analysis, particularly suited to complex onset flows (Thé and Yu, 2017; Storey et al.,

2016). Such studies have informed development of engineering tools for prediction of the time-varying loads and component load spectra (Moriarty and Hansen, 2005; Smilden et al., 2016) that are required for fatigue design. Similar information is required for tidal stream turbines for which the operating environment comprises a depth constrained turbulent flow, potentially with free surface waves, and for which the supporting structure is typically much larger, relative to the turbine, than for wind turbines. Experimental datasets provide a crucial basis for development of understanding of the processes contributing to component loading and for validation of numerical models. Tidal turbine loading and performance have been analysed for three-bladed horizontal axis turbine models of various diameter, (Bahaj, Batten and McCann, 2007; Kolekar and Banerjee, 2015; Gaurier et al., 2015; Payne, Stallard and Martinez, 2017). Several studies have also addressed unsteady loading of rotors or turbines due to waves, in towing tanks (Lust et al., 2013; Luznik et al., 2013; Galloway et al., 2014; Doman et al., 2015) and in flumes and tanks (Gaurier et al., 2013; de Jesus Henriques et al., 2014; Fernandez-Rodriguez et al., 2014; Martinez et al., 2017). The impact of turbulences on turbine performance and loading has also been explored (Chamorro et al., 2013; Mycek et al., 2014; Fernandez-Rodriguez et al., 2014; Milne et al., 2016; Blackmore et al., 2016). Durán Medina et al. (2017) carried out an in-depth analysis of the correlations between onset flow velocity and turbine power production based on spectral methods, empirical mode decomposition and time-dependent intrinsic correlation. However, there has, to-date, been limited in-depth analysis of the frequency variation of loading of horizontal axis tidal turbine blades and the turbine supporting structure. This work analy-

ses the relationship between the frequency variation of principal components of loading of a horizontal axis tidal stream turbine focusing on streamwise blade loading, thrust and power developed by the three-bladed rotor, and the streamwise and transverse loading on the entire turbine assembly comprising rotor, nacelle and tower.

The experimental approach and flow conditions studied are summarised in Section 2, variation of rotor and blade loading are investigated in Section 3 and factors leading to unsteady loading of the support structure are analysed in Section 4. Conclusions are provided in Section 5.

2. Experimental apparatus and considerations

2.1. Turbine model

The experimental turbine model used was a bed mounted three-bladed horizontal axis machine with a rotor diameter D = 1200 mm. The blade design was developed to produce a radial variation of the rotor thrust coefficient at a specific tip speed ratio similar to that of a full scale generic turbine (Stallard et al., 2015). The idea behind this approach is that highest rotor loads and wakes are phenomena which are predominantly affected by the thrust characteristics of turbines. The turbine model was developed to integrate a high level of instrumentation in order to measure the following quantities:

- streamwise root bending moment for each blade
- rotor torque

- rotor thrust
- rotor absolute angular position

A detailed description of the experimental model, of its design and manufacture can be found in Payne, Stallard and Martinez (2017) and a section view of the model is reproduced in Fig. 1.

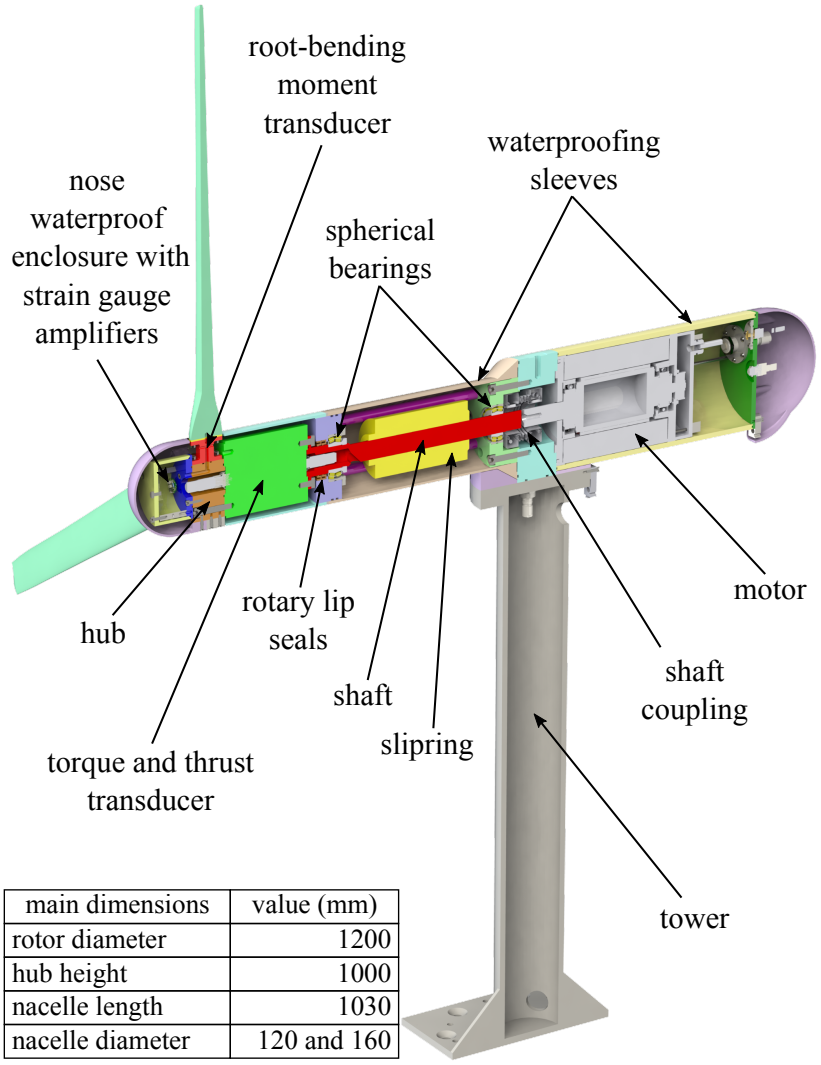

main dimensions	value (mm)
rotor diameter	1200
hub height	1000
nacelle length	1030
nacelle diameter	120 and 160

Figure 1: CAD section view of the experimental turbine model

A primary consideration for the model design was to maximise quality of load measurements. This approach was implemented by locating the sensors as close as possible to where the loads they are measuring are applied. When considering the load path, the sensors are located 'upstream' of the shaft rotary seals so that their associated parasitic friction does not affect the load measurements. As a consequence, these sensors are in a wet environment and so were designed to be waterproof. The turbine generator was simulated by a brushless servo motor controlled in speed.

The turbine model was installed so that the rotor axis was located at mid-depth (1 m deep). The bottom of the turbine tower was mounted to a fixed mooring structure via a six-axis load cell of the type TYPR FX2.6 manufactured by the company SIXAXES.

Signal from all turbine sensors (including the six-axis foundation load cell) were synchronously sampled at 256 Hz. Sample measurement time series can be found in Payne, Stallard and Martinez (2017).

2.2. Testing facility

The study was conducted in the flow recirculating facility of IFREMER in Boulogne-sur-Mer, France shown on Fig. 2(a). The flow channel is 4 m wide, has a usable length of 18 m and was operated at 2 m depth (Germain, 2008). The blockage ratio, taking into account the rotor, the tower and support structure is 0.2. The inlet of the flume is fitted with removable flow conditioning units (see Fig. 2(b)) which produced two levels of streamwise turbulence intensity TI_u: 3% with the flow conditioning units and 12%

without. TI_u is defined by:

$$TI_u = 100\frac{\sigma(u)}{\overline{u}} \tag{1}$$

where $\sigma(u)$ is the standard deviation of the streamwise velocity component u and $\overline{u}$ is the mean of u.

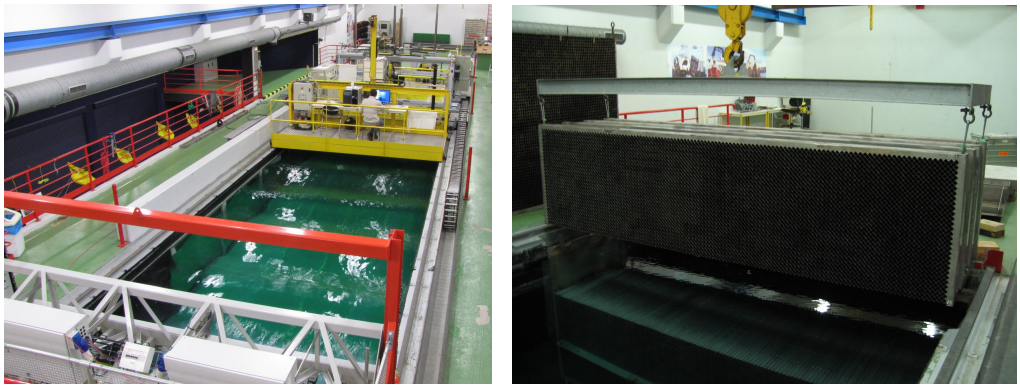

(a) (b)

Figure 2: IFREMER recirculating flow and wave facility 2(a) and its removable inlet flow conditioning screen 2(b) (images courtesy of IFREMER)

The facility is equipped with a two-component fibre optical laser Doppler anemometry (LDA) system consisting of a FiberFlow transmitter and manipulators made by Dantec and of two Genesis MX SLM series lasers produced by Coherent, one green (514 nm wavelength) and the other blue (488 nm wavelength). The LDA probe is mounted on a motorised gantry allowing automated movement in the vertical and cross flow directions.

Measurements were taken at turbine hub location in the absence of the

turbine. The streamwise mean velocity was $0.814\ \mathrm{m \cdot s^{-1}}$ for $TI_u = 3\%$ and $0.819\ \mathrm{m \cdot s^{-1}}$ for $TI_u = 12\%$. With LDA, the sampling frequency is not constant as measurements take place each time a seeding particle passes through the measurement volume. It is also different for the two velocity components measured. The mean sampling frequency for the high and low turbulence conditions were 283 and 941 Hz respectively in the streamwise direction and 71 and 258 Hz respectively in the transverse direction. The sampling durations were 256 and 200 s for the high and low turbulence conditions respectively. In order to carry out spectral analyses of flow velocities, the LDA timeseries are first re-sampled at a constant frequency corresponding to the mean sampling frequency of the timeseries. The re-sampling is applied using linear interpolation and alternative sampling frequencies were tested to ensure that the chosen frequency was sufficient to resolve the frequency range shown. Alternative methods to compute periodigrams without re-sampling, such as the Empirical Mode Decomposition - Hilbert Spectral Analysis lead to comparable results, as shown by Durán Medina et al. (2017) for the Empirical Mode Decomposition - Hilbert Spectral Analysis method. The spectral density of the velocity fluctuations with respect to the mean is shown in Fig. 3 for streamwise (u') and transverse (v') fluctuations for the two TI_u levels. The spectral densities are normalised by $\overline{u}^2$. The spectral density curves shown were obtained by averaging components over bins whose frequency widths are evenly distributed on a log scale. This means that high frequency bins contain a wider frequency range than low frequency bins which leads to curves being smoother toward higher frequencies. This processing was applied to all spectral density plots in this article. As expected, there is

higher turbulent kinematic energy density across the frequency range for the flow with higher turbulence intensity. For $TI_u = 12\%$, u' and v' spectra are relatively close, implying isotropic turbulence. However, for $TI_u = 3\%$, the flow is anisotropic with $u'/v' > 1$ for frequencies below 2 Hz and this ratio increases with decreasing frequency. This difference is due to the fact that for the low TI conditions, the flow enters the test section of the flume through a honeycomb structure (shown in Fig. 2(b)). This constrains the flow in the cross-flow direction, hence limiting variance of transverse fluctuations. In the inertial sub-range (at frequencies roughly above 1 Hz here) it can be seen that all curves have a slope which broadly follows the Kolmogorov minus five thirds power law. However towards the higher frequencies, u' at low TI departs significantly from that slope. This can be attributed to the anisotropy of the flow which implies that the Kolmogorov dissipation scale no longer fully applies (see Durán Medina et al. (2015) and Thorpe (2007)).

2.3. Reynolds and Froude numbers

The chord based Reynolds number associated with the blade profile at radius r is defined as follows:

$$Re_c(r) = \frac{\rho \cdot \lambda \cdot r \cdot \overline{u} \cdot c(r)}{\mu \cdot R} \tag{2}$$

where ρ is the water density, λ is the tip speed ratio (TSR), R is the rotor radius, $c(r)$ the blade chord length at radius r and μ the dynamic viscosity of water. For $r/R \geqslant 0.2$, $c(r)$ varies little with r compared with r/R (see table 2 of Payne, Stallard and Martinez (2017)). From (2) $Re_c(r)$ can therefore

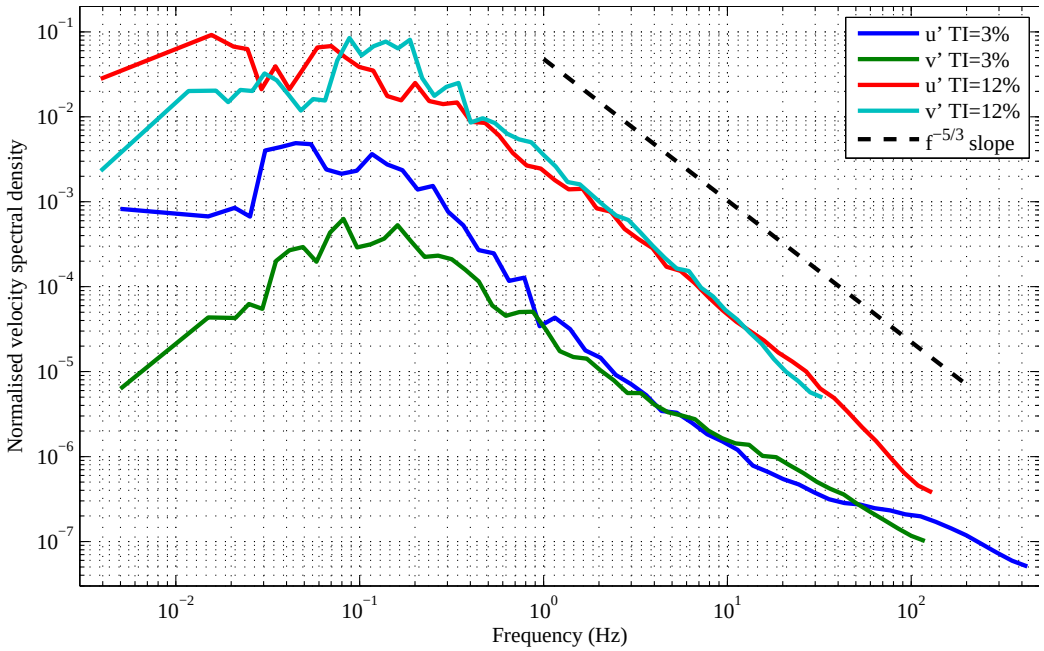

Figure 3: Normalised velocity spectral density in the streamwise (u') and transverse (v') direction for TI=3 and 12% (TI=3% data are courtesy of IFREMER)

be assumed to be a linear function of r for $r/R \geqslant 0.2$. For the experiments reported herein where TSR ranges from 4.5 to 7 and for $r/R \geqslant 0.2$, $49\,000 \leqslant Re_c \leqslant 252\,000$.

The rotor diameter based Reynolds number is given by:

$$Re_D = \frac{\rho \cdot \overline{u} \cdot 2R}{\mu} \tag{3}$$

$Re_D = 975\,000$ throughout this article.

The Froude number of the test channel is defined by:

$$Fr = \frac{\overline{u}}{\sqrt{gh}} \tag{4}$$

where g is the gravitational acceleration and h the channel water depth. For the experiments reported in this article, $Fr = 0.18$.

2.4. Root bending moment sensor quality check

Each blade was mounted to the hub through a root bending moment sensor. More details on the sensor design and calibration can be found in Payne, Stallard and Martinez (2017). As noted previously by the authors, the sensors developed a slow drift fault during the initial test programme. That drift progressed slowly, so providing that the signal remained within the saturation limits of the amplifier and that the sensors were 'zeroed' several times per day, measurements were deemed to be accurate within the 5% band established through calibration, especially for investigating the fluctuating component of the load. For time series which met this quality criteria, agreement between the streamwise force on the rotor inferred from the root bending sensor and the rotor thrust measured directly at the shaft was checked. The root bending moment sensors measure bending moment on the blades in the streamwise direction. The corresponding streamwise force on the blade is a function of the radial position of the centroid of the streamwise load on the blades. This 'lever arm' distance cannot be measured experimentally and was instead estimated with a blade element moment (BEM) theory model. The BEM tool is as described in Hansen (2008), with Spera high axial induction factor correction. The lever arm distance obtained by this method (see Payne, Stallard and Martinez (2017)) varies only by 2.3% over the tip speed ratio (TSR) range 4.5 to 6.0 and a constant value of 330 mm was therefore used to infer the mean streamwise force on the blade from the mean of

the root bending moment signal. Comparison is shown in Fig. 4 for tests at $TI_u = 3\%$. The discrepancy varies little (between 13 and 15%) over the TSR range and can therefore be considered as consistent. The discrepancy itself is not surprising and can be attributed to the following factors.

- The lever arm distance is computed using a standard BEM approach which does not account for the blockage factor (14%), onset flow profile or flow turbulence, which are all present in the physical experiment.
- Due to space restrictions, the geometry of the flexure of the root bending moment sensors was that of a beam. Flexure deflection is mainly driven by bending moment but the sensor is also, to a lesser degree, affected by shear force to the extent that calibration exhibited a maximum error of 5% (Payne, Stallard and Martinez, 2017).

3. Rotor loads

The rotor loads are partly analysed using the standard thrust and power coefficients which are defined respectively by:

$$C_T = \frac{T}{\frac{1}{2} \cdot \rho \cdot A_r \cdot \overline{u}^2} \quad \text{and} \quad C_P = \frac{Q \cdot \overline{\omega}}{\frac{1}{2} \cdot \rho \cdot A_r \cdot \overline{u}^3} \tag{5}$$

where T is the rotor thrust, Q its torque, $\overline{\omega}$ its averaged rotational speed and A_r the rotor area.

3.1. Angular dependency

In order to investigate the impact of the absolute angular position of the rotor on its thrust loads, measurements from sensors are binned into 360 angular sectors (each 1° wide) based on the rotor absolute angular position at

the time of the measurement. Values in each bin are then averaged to yield 'phase-averaged' measurements for each 1° sector of the rotor full revolution. Figure 5 shows the relative variation (in percent) with respect to the mean of those 'phase-averaged' measurements plotted in polar coordinates.

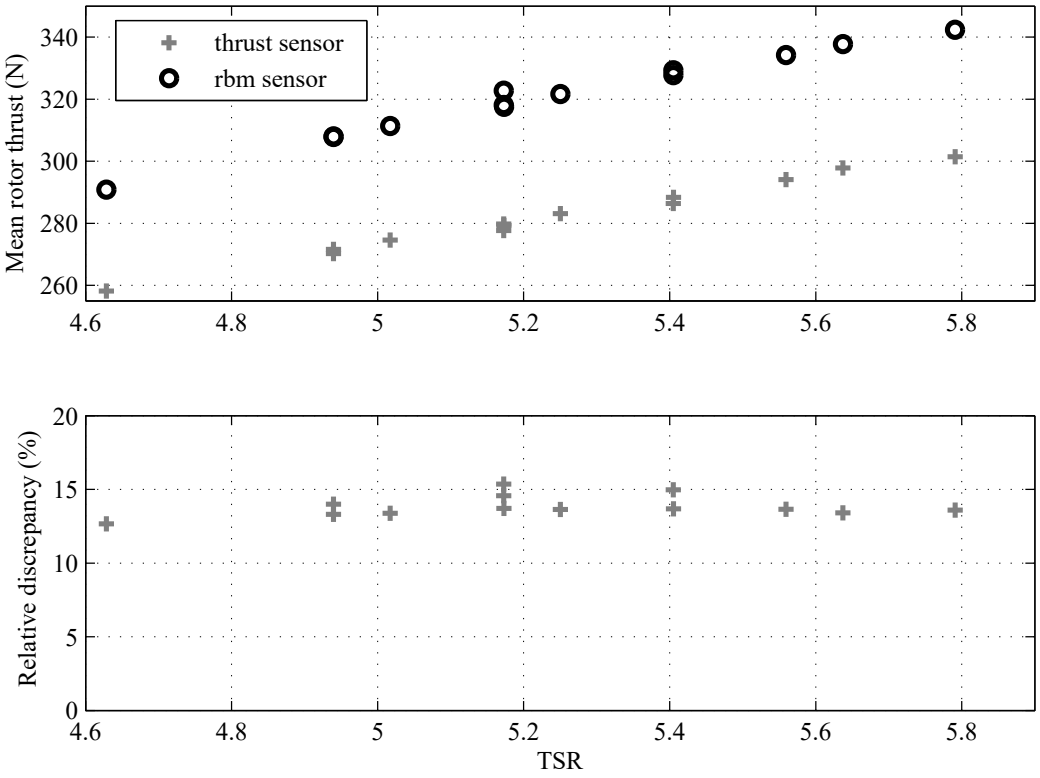

Figure 4: Comparison between mean rotor thrust measured with the torque and thrust transducer and inferred from the blade root bending moment (rbm) sensors (top graph). The bottom graph shows the corresponding relative discrepancy with respect to the torque and thrust transducer measurements. Measurements were carried out over a range of tip speed ratios with an onset flow velocity of $0.814\ \mathrm{m \cdot s^{-1}}$ and a $TI_u = 3\%$.

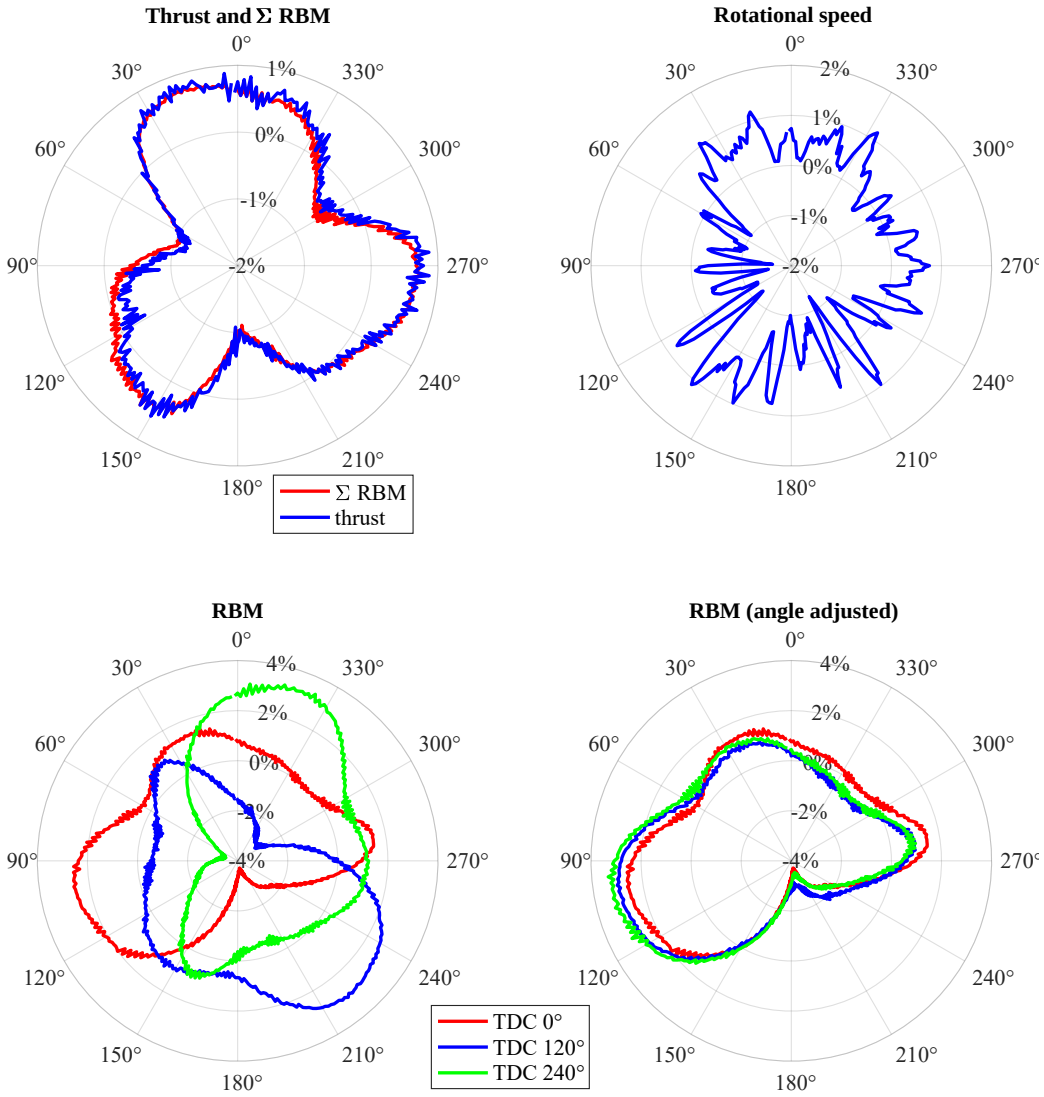

Figure 5: 'phase-averaged' rotor loads and rotational velocity variations (in %) plotted against rotor absolute angular position. Σ RBM corresponds to the sum of the measurements from the three root bending moment (RBM) sensors. The legend for the two bottom plots indicates the absolute angular position of the rotor when a given blade is at top dead centre (TDC). In the bottom right plot, the angular positions for two blades have been adjusted by 120° and 240° respectively to directly compare the azimuthal variation of the root bending moment on each blade. Measurements were carried out with an onset flow velocity of 0.814 $\mathrm{m \cdot s^{-1}}$, $TI_u = 3\%$ and TSR = 6.9.

Azimuthal variation of thrust is in close agreement with the sum of the three root bending moment signals (see top left frame) and this provides further confidence in the root bending moment quality control process of Section 2.4. The variations of the thrust (and Σ RBM) curve are overall small (within a 2% range) but two clear patterns can be observed. The first pattern is exhibited by three distinct lobes about 120° apart, which is believed to be associated with the tower shadowing effect. The second pattern is a small distortion of the three lobe pattern with mainly the part of the lobe in the 60° to 120° sector being slightly smaller than for the two other lobes. This pattern, which takes place once per revolution, is also observed in figure 8 of Section 3.2 on frequency analysis (peak A taking place at frequency f_0). This is correlated with the angular variation of the rotor rotational velocity (see top right frame) which indicates a lower speed in the 60° to 120° region. Given that the onset flow velocity remains constant, this translates into a lower TSR which, in turns, yields a lower thrust as can be seen on the C_T versus TSR curve shown in figure 6. This rotational velocity variation is believed to be due to either a mechanical artifact of the drive train or something to do with the motor speed control.

The two bottom frames show the variations in root bending moment experienced by each blade. It can be seen that the three curves are, as expected, similar and that when no angular position adjustment is applied (bottom left graph) they are 120° apart. Those two plots show very clearly the sharp dip in root bending moment associated with the tower shadowing effect. It can be seen that this minimum does not occur exactly when

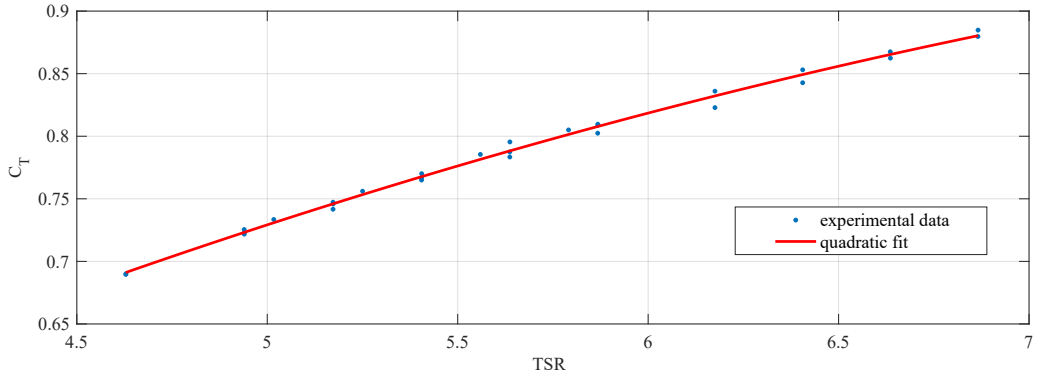

Figure 6: C_T versus TSR curve obtained by a quadratic fit on experimental data measured with an onset flow of 0.814 $\mathrm{m} \cdot \mathrm{s}^{-1}$ and TI=3%.

the blade passes the tower (180° on the bottom right plot) but that there is a lag of around 15°. Occurrence of this lag is consistent with observations from CFD studies (Mason-Jones et al., 2013), (McNaughton, 2013) and from measurements from full-scale prototype trials (Ahmed et al., 2017), although with some difference of magnitude between each case due to differences of turbine operating point and geometry, including position of tower relative to rotor plane. Beyond the tower shadowing effect, there are other significant variations in root bending moment over the full rotor revolution, especially in the transverse direction. To understand these better, it is useful to look at the variation in onset flow velocity over the flume cross section. Figure 7 shows the variation of the streamwise velocity with respect to the hub velocity over the flume cross section where the turbine was deployed but in the absence of the turbine. The measurements do not quite cover the whole area of the rotor (indicated by the black circle) but a transverse asymmetry is clearly visible and consistent with the similar asymmetry in root bending moment loads observed in figure 5. The transverse asymmetry in the flow is

due to the fact that it is generated by two impellers, located side by side in the bottom recirculation channel of the flume, which are both spinning in the same direction (see Germain (2008) for further detail on the flume layout). The flow conditioning units fitted to the flume reduced the transverse flow asymmetry to some extend but did not suppress it completely.

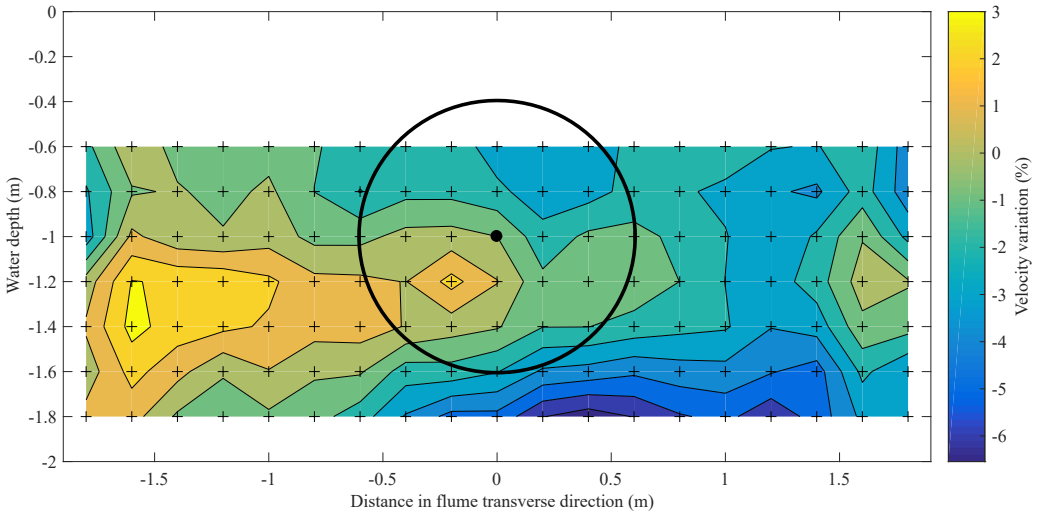

Figure 7: Velocity variation map across the section of the flume at the location where the turbine was deployed but in the absence of the turbine. The velocity variations (in %) are calculated with respect to the hub velocity ($0.814\,\mathrm{m}\cdot\mathrm{s}^{-1}$) measured at the location indicated by the black dot. The circle corresponds to the location of the turbine rotor and the crosses are the measurement points (raw velocity data courtesy of IFREMER)

3.2. Thrust and torque loads frequency analysis

Frequency dependency of rotor loads are first investigated considering the spectral density of the thrust and power coefficients defined by equation (5). These spectral densities S_{C_T} and S_{C_P} are plotted in Figs 8 and 9 for the

two different turbulence intensity regimes and also for when the turbine is rotating under dry test conditions, in air. The spectra are plotted against frequency normalised by the rotor rotational frequency f_0. The rotor is spinning at 80 RPM, corresponding to TSR values of 6.14 and 6.18 for $TI_u = 3\%$ and $TI_u = 12\%$ respectively. The time series durations used to compute these spectral densities are 256, 128 and 3584 s for the dry test, the low and high turbulence conditions respectively. The normalised spectral density of the streamwise flow velocities of Fig. 3 are also shown.

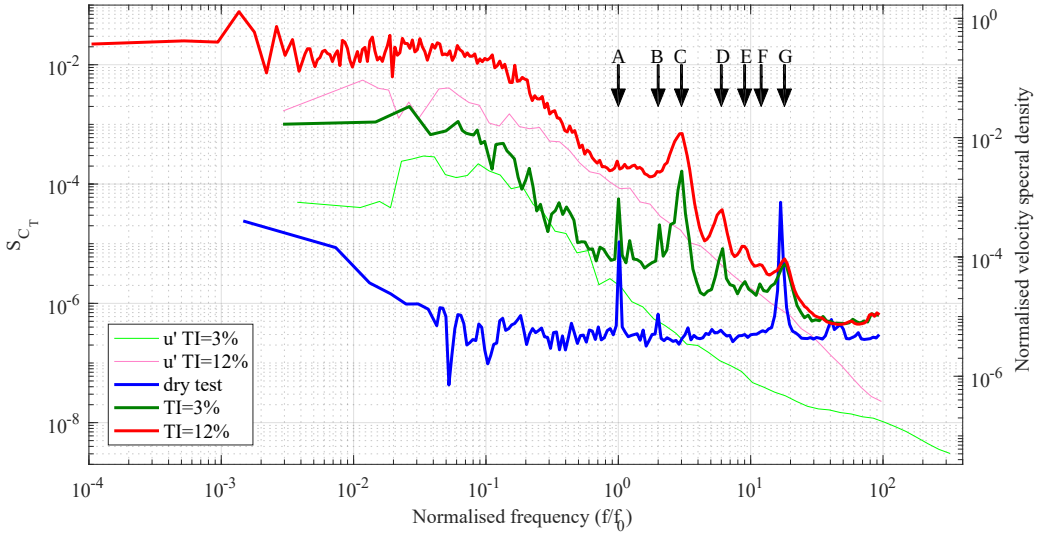

Figure 8: Spectral densities of C_T (thick lines, left hand side vertical axis) and normalised velocity spectral density (thin lines, right hand side vertical axis) plotted against frequency normalised by turbine rotational frequency f_0.

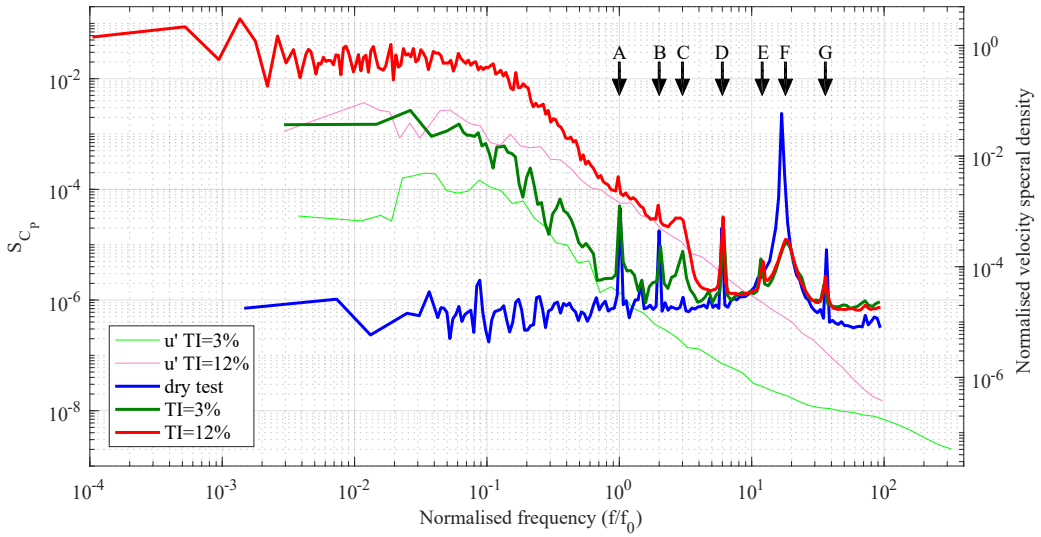

Figure 9: Spectral densities of C_P (thick lines, left hand side vertical axis) and normalised velocity spectral density (thin lines, right hand side vertical axis) plotted against frequency normalised by turbine rotational frequency f_0.

For both turbulence intensity values studied, the general trend of the curves of thrust S_{C_T} and power S_{C_P} spectra are similar. For $f/f_0 < 1$ both curves (3% and 12% TI as green and red curves respectively) are approximately parallel to each other and roughly in-line with the velocity spectral density for the same turbulence intensity. The slope of the thrust coefficient spectra is similar to that of the velocity spectra. However, the slope of the power coefficient spectra is steeper than that of the onset velocity spectral density in the inertial sub-range. A similar observation was also reported by Durán Medina et al. (2015) who suggest that this may be related to maintaining rotor velocity constant through speed control. Nevertheless, Fig. 8 and 9 show a clear correlation between the velocity fluctuation in the onset flow and the thrust and torque loads with the TI = 12% load curves consis-

tently above their TI = 3% counterparts by about one order of magnitude. As the frequency increases ($f/f_0 > 1$) the load spectra converge and tend to a plateau at high frequency, departing from the trend of the velocity spectral density. This plateau is thought to be due to background noise associated with the sensors. This is corroborated by the fact that the level of the plateau is independent of the turbulence intensity of the flow.

Multiple specific peaks are observed in the S_{C_T} spectra for both turbulence intensities. For the sake of convenience these have been labeled in Fig. 8. The highest peak for both curves is peak C, which takes place at three times the rotational frequency. This is due to the shadowing effect of the tower, taking place when each blade passes the tower i.e. three times per rotor revolution. Peaks D, E and F take place at $6f_0$, $9f_0$ and $12f_0$ respectively and their amplitude decreases with increased frequency indicating that they are harmonics of the $3f_0$ peak. Peak A, B and G take place respectively once, twice and 18 times per revolution and could not be explained by any obvious hydrodynamic phenomenon. It was therefore decided to investigate S_{C_T} with the turbine model taken out of the flume ('dry test') which corresponds to the thick blue line in Fig. 8. The general trend of that curve is flat since there cannot be any correlation with onset flow velocity fluctuations and this is indicative of the flat, broad band noise floor inherent to the sensor. The S_{C_T} values appear to increase at the lowest frequencies. This is believed to be due to noise in the spectral density whose computation for low frequencies involves no or only little averaging (as explained in section 2.2). The curve exhibits two clear peaks (labeled A and G). Peak A occurs once per revo-

lution and is attributed to a mechanical artifact of the turbine model drive train, e.g. a slight misalignment between the motor and turbine shafts or a slight imbalance in the rotor. It can be seen that this affects S_{C_T} for TI = 3% and to a much lesser extent at TI = 12%. This makes sense as ambient level of load fluctuation is significantly higher for TI at 12% than at 3%. Peak B is lower than peak A and appears to be a harmonic of peak A. Peak G occurs at $18f_0$ and, as this is quite high for a mechanical artifact, this is thought to be either due to vibration induced by pole cogging in the motor or a function of the motor speed controller or possibly some electromagnetic interference. Irrespective of the phenomenon at play, it is an artifact of the turbine model itself and not of its interaction with the flow. However, it is evident that it is affecting the S_{C_T} curves corresponding to the turbine in the flume on which peak G is clearly of higher magnitude than a harmonic of the lower frequency hydrodynamic forcing.

The analysis of the peaks in the S_{C_T} curves of Fig. 8 broadly also applies to the S_{C_P} curves of Fig. 9. However, peak C is of different magnitude and further peaks are observed (D, E and G). The peak associated with the tower shadowing effect (peak C) is less pronounced than for S_{C_T} which can be explained by the fact that this phenomenon is mainly a streamwise wake effect and affects therefore more significantly rotor thrust than torque. The 'dry test' S_{C_P} curve exhibits three extra peak (D, E and G) compared with its S_{C_T} counterpart. The reason for peak D, which takes place at $6f_0$, is not fully understood but is obviously a 'dry' phenomenon associated with the turbine model. It nevertheless clearly affects S_{C_P} when the turbine is in the

flow. Peak E occurs at $12f_0$ and is believed to be a harmonic of peak D. Peak F takes place at $18f_0$ and corresponds to peak G in Fig. 8. Peak G (of Fig. 9) occurs at $36f_0$ and is believed to be a harmonic of peak F.

3.3. Frequency variation of blade root bending moment

As mentioned in section 2.1, each turbine blade is fitted at its root with a sensor measuring fluctuation of bending moment due to the streamwise load (contributing to thrust) experienced by the blades. The root bending moment (RBM) signals are rendered dimensionless using a similar approach as for the thrust coefficient C_T (see (5)):

$$C_{RBM} = \frac{RBM}{\frac{1}{3} \cdot D \cdot \left(\frac{1}{2} \cdot \rho \cdot A_r \cdot \overline{u}^2\right)} \tag{6}$$

where D is the rotor diameter and the other symbols are the same as for equation (5). Figure 10 shows the spectral densities of C_{RBM} for each blade. It can be seen that the load spectra are nearly identical for all blades, except for small discrepancies at both ends of the frequency spectrum. At high frequency, the difference is likely to be due to slight mechanical and/or electronic inconsistencies of the RBM_2 sensor with respect to the two others, leading to a higher background noise level.

With the consistency in spectral density of the root bending moment established across all three blade sensors, the relationship between spectra of velocity, of blade loading and of rotor loading is now considered. Figure 11 compares the spectra of C_{RBM_1} (corresponding to blade 1 only) with that of C_T, with the normalised velocity spectral density of the onset flow (u') and

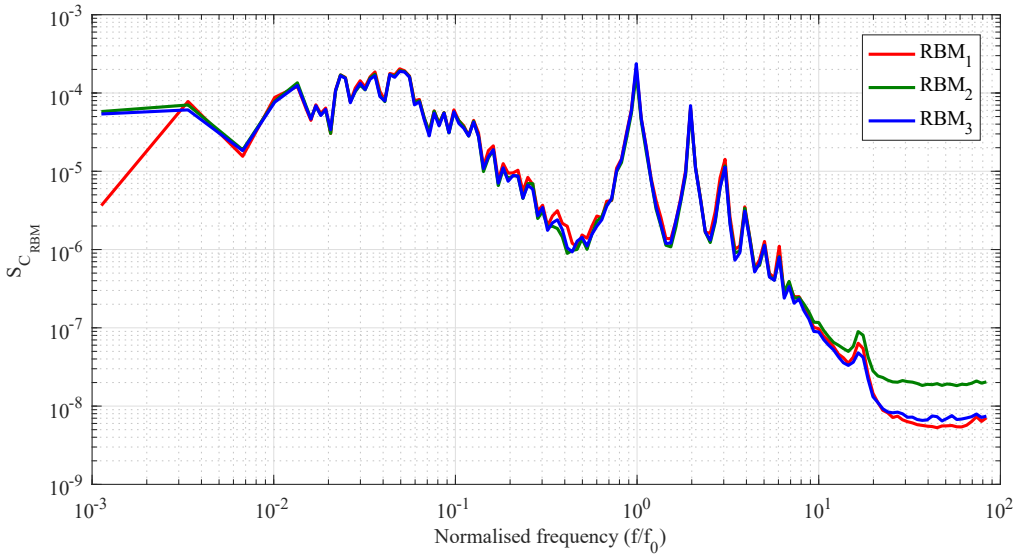

Figure 10: Spectral density of C_{RBM} for the three rotor blades plotted against frequency normalised by turbine rotational frequency f_0. The onset flow has a TI=3% and the TSR = 6.9 (rotor speed: 89 rpm). The sampling duration is 600 s.

with the spectral density of $C_{\Sigma RBM}$ defined as follows:

$$C_{\Sigma RBM} = \frac{\sum_{i=1}^{3} RBM_i}{D \cdot \left(\frac{1}{2} \cdot \rho \cdot A_r \cdot \overline{u}^2\right)} \tag{7}$$

where suffix i is the blade index. $\sum_{i=1}^{3} RBM_i$ corresponds to the summation of the three root bending moment time series. In other words, at each time step, the three root bending moments measured simultaneously for the three blades are added together. To facilitate visual comparison of the trend between the C_T and RBM curves, the spectral density of C_T is shown multiplied by 0.05. Curve peaks have also once again been labeled for convenience.

Over the low frequency range, both the C_{RBM_1} and $C_{\Sigma RBM}$ curves follow

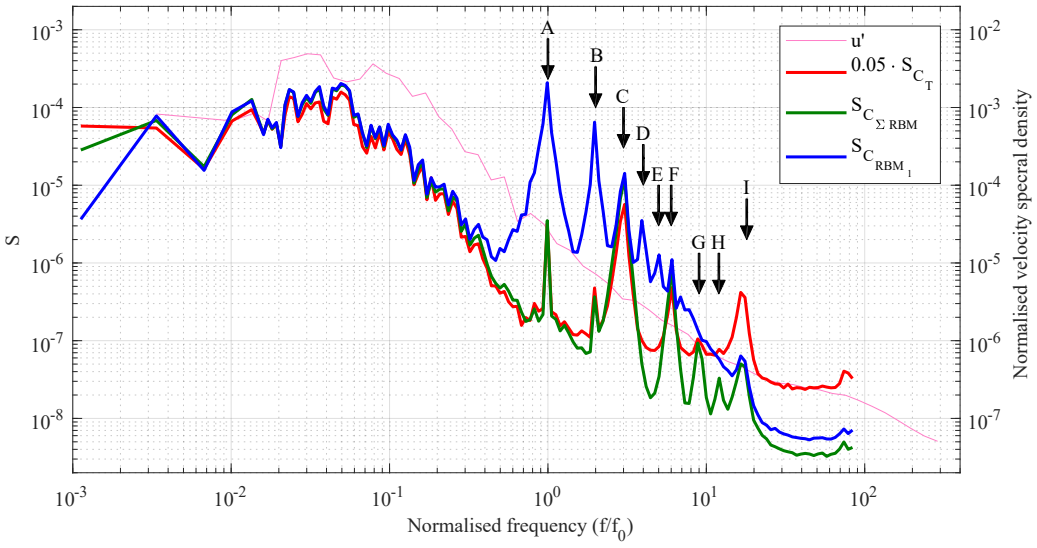

Figure 11: Comparison between spectral densities of C_{RBM_1}, C_T and $C_{\Sigma RBM}$. S_{C_T} is multiplied by 0.05 to shift its curve vertically and facilitate comparison to the RBM curves. The normalised velocity spectral density of the onset flow u' is also plotted on a different vertical scale (right axis). All quantities are plotted against frequency normalised by turbine rotational frequency f_0. The onset flow has a TI=3% and the TSR = 6.9 (rotor speed: 89 rpm). The sampling duration is 600 s.

the same trend as the velocity spectrum indicating that root bending moment loads are strongly correlated with turbulence of the onset flow. However, the spectrum associated with rotor loads ($C_{\Sigma RBM}$) is correlated with the onset flow to a higher frequency (for $f/f_0 \leqslant 1.5$ aside from a narrow spike at $f/f_0 \simeq 1$) than that of an individual blade (for $f/f_0 \leqslant 0.5$).

For $f/f_0 > 0.5$ the C_{RBM_1} curve exhibits a series of sharp peaks (labeled A to F) of decreasing amplitude and whose frequencies correspond to $f/f_0 = 1$, 2, 3, 4, 5 and 6 respectively. Peak A is expected to be due to the

tower shadowing effect which affects each blade once per rotor revolution. This has a similar amplitude to that of the low frequency turbulence induced loads. The frequencies and amplitudes of peaks B to F suggest that they are harmonics of peak A.

The main peak exhibited by the $C_{\Sigma RBM}$ curve is at $3f_0$ (peak C) corresponding to the tower shadowing effect on each blade once per revolution. Peaks F, G and H on that curve, taking place respectively at $6f_0$, $9f_0$ and $12f_0$ are harmonics of peak C. Peaks A, B and I of the $C_{\Sigma RBM}$ curve are not believed to be due to hydrodynamic phenomena but to mechanical and/or motor artifacts (see figure 8 and Section 3.2).

There is agreement between the spectra of thrust and of sum of root bending moment sensors over much of the frequency range (to about $3f_0$) but the RBM sensors have a lower noise floor and so capture greater detail on the frequency dependency to about $20f_0$. Over this range, the distinct three harmonics of peak C are observed (peaks F, G and H).

Figure 12 compares the spectral density of C_{RBM_1} for the two levels of onset flow turbulence intensity (3% and 12%) and also shows the normalised velocity spectral density of the corresponding onset flows. The vertical gap between the two C_{RBM_1} curves is qualitatively consistent with that between the velocity spectral density curves. The frequency at which blade loading becomes uncorrelated with the onset flow spectrum is around $0.6f_0$. This is slightly higher than observed in Figure 11 and this is likely to be due to the

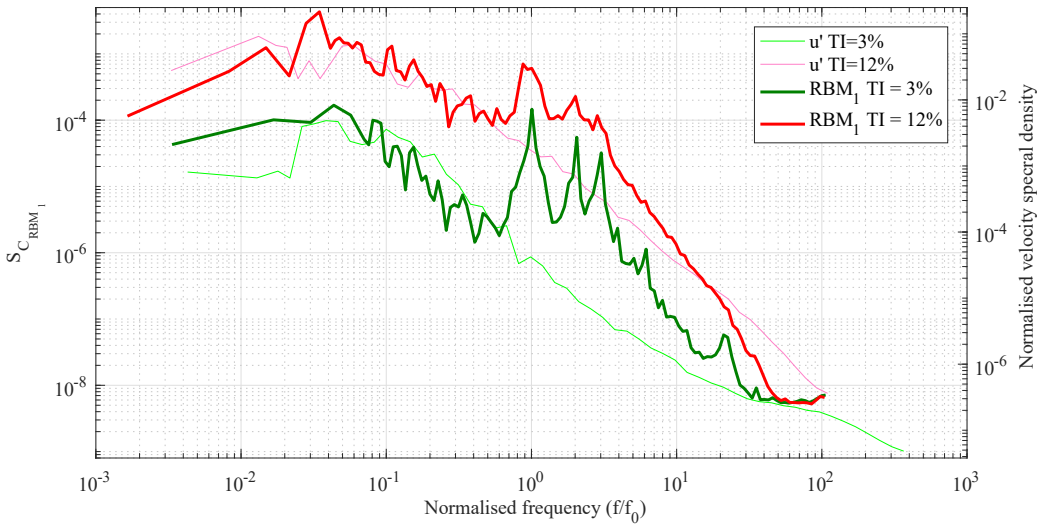

Figure 12: Spectral densities of C_{RBM_1} in onset flows of turbulence intensity of 3% and 12% for TSR = 5.4. The normalised velocity spectral densities of the onset flow u' for both levels of turbulence are also plotted on a different vertical scale (right axis). All quantities are plotted against frequency normalised by turbine rotational frequency f_0. The sampling durations for the RBM measurements are 128 s and 256 s for the low and high turbulence intensity conditions respectively.

different operating point (see related discussion in Payne, Stallard, Mullings and Martinez (2017), Chamorro et al. (2013)). It can be seen that for the flow with higher turbulence intensity, the peaks of the blade loading spectrum associated with the effects of the turbine structure are less pronounced. This is believed to be due to the higher level of turbulence induced loads which reduces the apparent amplitude of the peaks. Qualitatively, similar behaviour has been observed through CFD simulation with a time-varying turbulent onset velocity field imposed to represent similar magnitude of turbulence (Ahmed et al., 2017). For frequencies greater than the third harmonic of the tower shadowing effect, the slope of blade loading spectra is steeper than

that of the corresponding velocity spectra. For TI = 3% this rapid decay is obscured by the narrow spike at $20f_0$ and by the sensor noise floor. However, for TI = 12% a similarly steep slope is observed over a wider frequency range before the sensor noise floor is reached, resulting in lower variance over frequencies greater than $20f_0$ than would be expected if loads were correlated with the onset velocity spectral density over this high frequency range.

4. Loads on support structure

To the authors' knowledge, in previously reported experimental investigation of horizontal axis tidal turbine, thrust loads were measured either at the level of the nacelle or at the base of the supporting structure. Typical examples of the former are Bahaj, Molland, Chaplin and Batten (2007) and Milne et al. (2013) where the thrust sensor spins with the shaft and is located between the hub and the component simulating the generator. Kolekar and Banerjee (2015) employed a slightly different approach with a static thrust sensor located at the back of the nacelle, between the motor and the support structure. On the other hand Gaurier et al. (2015), de Jesus Henriques et al. (2014), Mason-Jones et al. (2012) and Stallard et al. (2015) estimate thrust loads using a load cell located above waterline on the supporting tower. The latter approach cannot isolate thrust on the rotor alone from loads on the nacelle and support structure as is pointed out in Gaurier et al. (2015). McTavish et al. (2014) adopted an interesting technique to mitigate this issue by enclosing the turbine tower (which is connected to the load cell) into a hollow tube held rigidly but not mechanically connected to the tower or the load cell. This way, the tower does not experience any drag. This method

does not however suppress the contribution of the drag on the nacelle to the thrust measurements.

In this experiment, the model was fitted with a torque and thrust transducer located between the shaft and the hub, and the entire turbine and support structure assembly was mounted on a six-axis load cell at the base of the tower. Data from this arrangement provided the opportunity to compare thrust loads experienced by the rotor alone with those acting on the turbine as whole. Such a comparison for mean load values over a range of TSR is shown in Fig. 13. The vertical position of the centroid of the streamwise force is also computed, using both F_x and the moment along the transverse axis M_y" from the load cell and this is shown in the bottom frame.

As would be expected, Fig. 13 clearly shows that the mean streamwise force F_x on the overall turbine exceeds the mean thrust load on the rotor alone. The standard deviation of turbine force F_x is also larger than that of shaft thrust. This can be explained by the fact that the main additional contribution to F_x compared to rotor thrust loads is drag on the tower. The tower is located in the near wake of the rotor (0.4D downstream) and is therefore subjected to a more turbulent flow than the rotor itself. This leads to more variability in the tower drag force than in the rotor thrust, hence the larger standard deviation in F_x than in thrust.

Mean force on the rotor is around 10% less than the mean force on the turbine. However this disparity (middle graph) decreases with increasing TSR. To understand this trend, it is useful to consider BEM theory, as derived

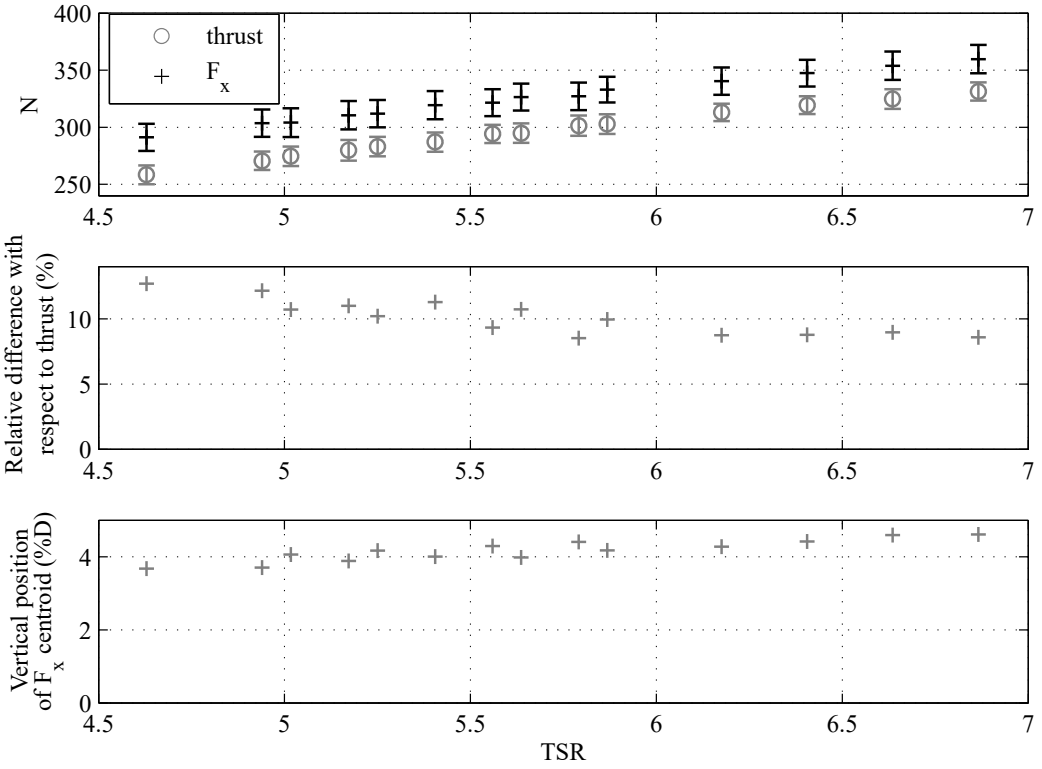

Figure 13: Comparison between thrust loads on the rotor alone and the overall streamwise force F_x on the turbine model (top graph). The error bars correspond to the standard deviation. The middle graph shows the discrepancy between the two measurements relative to thrust. The bottom graph shows the vertical position of the centroid of F_x with respect to the rotor axis. This position is normalised by the rotor diameter D and given in %. Measurements were carried out over a range of tip speed ratios with an onset flow velocity of $0.814\ \mathrm{m \cdot s^{-1}}$ and a $TI_u = 3\%$.

in detail in Hansen (2008) (chap. 4), which implies that:

$$T \propto a \cdot (1 - a) \cdot u^2 \tag{8}$$

where T is the rotor thrust, a the axial induction factor, u the onset velocity and $\propto$ means "proportional to". The streamwise flow velocity u_1 directly in the wake of the turbine is given by:

$$u_1 = (1 - 2 \cdot a) \cdot u \tag{9}$$

Given that the drag force F_D on the tower is proportional to u_1^2:

$$F_D \propto (1 - 2 \cdot a)^2 \cdot u^2 \tag{10}$$

Combining (8) and (10) yields after simplification:

$$\frac{F_D}{T} \propto \frac{1}{a \cdot (1 - a)} - 4 \tag{11}$$

From BEM, the right-hand side of (11) decreases with TSR which is consistent with the middle graph of Fig. 13.

The bottom graph of Fig. 13 shows that the vertical position of the centroid of F_x is slightly above the rotor axis, even though the streamwise loads on the tower are applied below the rotor axis. This is the case because F_x is dominated by rotor thrust and the thrust on individual blades (see Fig. 5 (bottom right)) is larger whilst blades are rotating through the upper half of the depth.

It is also interesting to compare rotor thrust and turbine loading in terms of spectral density. Fig. 14 shows the spectral density of these forces together

with that of the transverse force F_y due to the whole turbine as measured by the load cell. Although the area on which force acts differs, all three forces are normalised by $\frac{1}{2} \cdot \rho \cdot A_r \cdot u^2$ (where A_r the rotor area) to facilitate comparison.

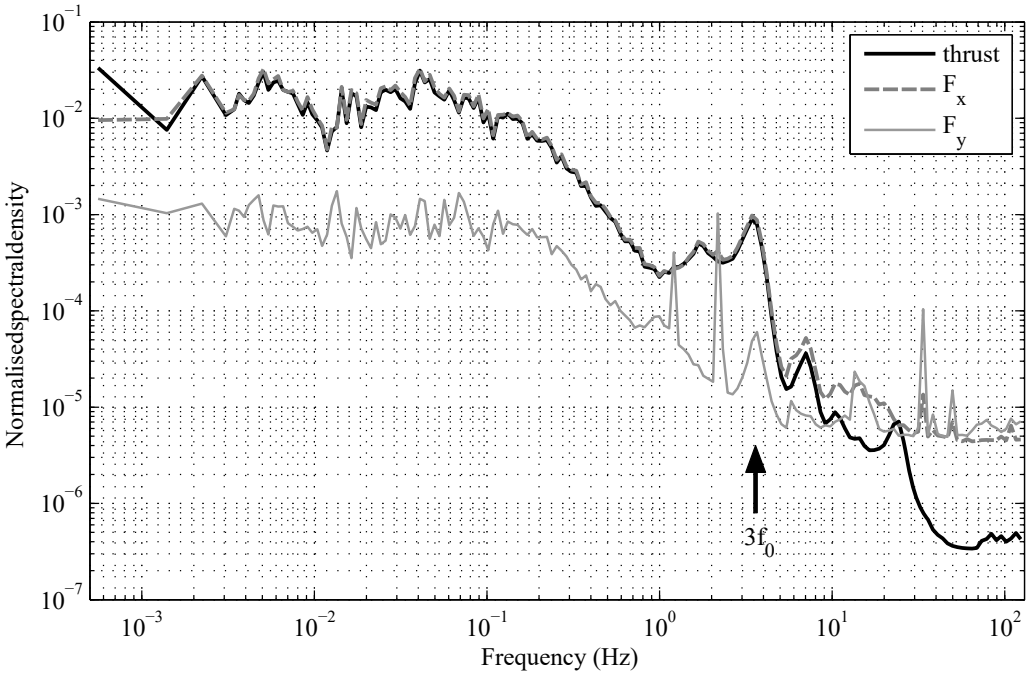

Figure 14: Spectral comparison of rotor thrust, overall streamwise (F_x) and transverse (F_y) forces. Measurements were carried out with a free stream velocity of $0.819\ \mathrm{m \cdot s^{-1}}$, $TI_u = 12\%$, TSR $= 5.53$ and the sampling duration is 3584 s. f_0 is the rotational frequency of the turbine.

For frequencies less than 5 Hz, turbine streamwise loading (F_x) is nearly identical to rotor thrust. For higher frequencies the F_x spectrum is of higher magnitude than the rotor loading spectrum. This is partly due to the higher noise floor of the load cell ($\sim 5 \times 10^{-6}$ for both F_x and F_y components reached

at about 30 Hz) compared to the thrust sensor ($\sim 4 \times 10^{-7}$ reached at 60 Hz). The F_y curve is consistently lower than the F_x one despite the fact that the flow is nearly isotropic, with the level of turbulence similar in the x and y directions, as can be seen in figure 3 ($TI_u = 12\%$). This is partly due to the disparity between projected area of the tower and nacelle associated with transverse force and the much larger swept area of the rotor which determines the rotor thrust.

All the major peaks of the thrust curve are explained in section 3. The F_y curve exhibits a peak at the blade frequency ($3f_0$) which is most likely due to the tower shadowing effect. The two narrow peaks, at 2.18 and 1.21 Hz do not appear on the thrust or F_x curves. These can be associated with vortex shedding behind the tower which is subjected to two flow regimes; the rotor wake across the upper portion and the bypass in the portion below the swept area of the rotor. To assess whether this is due to shedding the normalised shedding frequency is considered. Rearrangement of the Strouhal number yields the streamwise velocity u_{tow} to which the tower is subjected:

$$u_{tow} = \frac{f_{tow} \cdot D_{tow}}{St} \tag{12}$$

where f_{tow} is the frequency of oscillation of the vortices, D_{tow} the tower diameter and St the Strouhal number. Streamwise velocity in the turbine wake was measured in the vertical plane above the turbine axis at 0.5D downstream of the rotor and is reported in Payne, Stallard and Martinez (2017) (Fig. 18). This velocity varies from $0.5\ \mathrm{m \cdot s^{-1}}$ to $0.9\ \mathrm{m \cdot s^{-1}}$ from the wake to the bypass region. The tower is actually located 0.4D downstream of the rotor and below the turbine axis where the wake and bypass velocities

might be slightly different than the ones measured above. However, assuming $0.5 \leqslant u_{tow} \leqslant 0.9\,\mathrm{m \cdot s^{-1}}$ is a reasonable starting point to estimate the Strouhal numbers for each section of the tower. For this velocity range the Reynolds number of the flow incident to the tower, Re_{tow}, is in the range $5.1 \cdot 10^4 \leqslant Re_{tow} \leqslant 9.1 \cdot 10^4$. The Strouhal number varies little for Reynolds numbers ranging from $3 \cdot 10^4$ to $2 \cdot 10^5$ and is equal to 0.19 (Bearman, 1969). With these numbers, (12) yields $u_{tow} = 1.17\,\mathrm{m \cdot s^{-1}}$ and $0.7\,\mathrm{m \cdot s^{-1}}$ which are slightly higher but reasonably close to the velocities which can be expected in the bypass flow and rotor wake respectively. The $1.17\,\mathrm{m \cdot s^{-1}}$ velocity corresponds to $Re_{tow} = 1.2 \cdot 10^5$ which is also within the range for which the Strouhal number is stable at 0.19. This strongly suggests that the peaks in F_y at 2.18 and 1.21 Hz are indeed due to vortex shedding on the tower with the different frequencies associated with the velocities of the bypass flow and wake respectively.

The support structure considered here is a simple cylinder. Developers may consider different forms, such as for reduced drag and hence reduced momentum extraction or for structural requirements. For design of both blades and supporting structures, consideration should be given to the impact of the unsteady loads due to onset flow and the support structure shedding regimes on fatigue design and avoidance of coincidence with driving forces at harmonics of the rotor frequency.

5. Conclusions

Unsteady loading of a three-bladed horizontal axis turbine has been analysed. The system studied comprises a three bladed rotor on a bed mounted support structure subject to a nearly uniform onset flow. The frequency variation of unsteady loads on the rotor, the supporting structure and the blades are analysed and related to characteristics of the turbulent onset flow and of the turbine.

For low frequencies, the spectra of blade loading, of rotor thrust and of the streamwise force on the turbine are correlated with the spectrum of the streamwise onset velocity. However, a steeper slope is observed for the spectra of power coefficient. Correlation of streamwise load spectra with the onset velocity spectra occurs up to a frequency equal to half the rotational frequency for blade loading, but to around three times this frequency for the rotor loading. For low onset turbulence (3% turbulence intensity) blade loading peaks are clearly observed at the rotational frequency and at five higher harmonics. This is associated with the tower-shadow affect with a reduction of blade load observed once per cycle when the blade is approximately 15-20 degrees misaligned with the tower. The amplitude of the peak at rotational frequency is similar to that of the highest onset flow induced loads at low frequencies. Similar fluctuations of load are observed when aggregated across the three blades and in the rotor thrust spectrum, with each harmonic at three times that of the blade load. For higher value of onset turbulence (12% turbulence intensity) blade loading is observed at the rotational frequency and the first two harmonics but with greater variation at intervening frequen-

cies. For the high frequency range, greater than fifth and third harmonic for low and high turbulence cases respectively, the slope of blade loading spectra is observed to be greater than that of the corresponding onset velocity spectra.

Although the turbine is bed-mounted and its tower is therefore generating drag force below the rotor axis, the centroid of the streamwise force over the entire turbine (rotor, nacelle and tower) is above the axis of rotation (by about 4% of the rotor diameter). This is mainly associated with the tower shadowing effect which reduces blade loads in the lower part of the rotor disc. Mean streamwise load on the nacelle and supporting structure is approximately ten percent of rotor thrust although this reduces slightly with increasing tip-speed ratio, due to variation of thrust and hence wake velocity over this range. Analysis of both streamwise and transverse force on the tower indicates that two vortex shedding regimes occur along the tower associated with the wake and bypass flow.

The analysis presented provides a benchmark for evaluating the capability of numerical models for unsteady load prediction.

Authors' Contributions

G.P. and T.S developed the turbine model specifications and design, the tank test programme and the analysis plan, G.P led the tank testing, the data analysis and drafted this manuscript, T.S was co-investigator on the project and contributed to the analysis presented and to manuscript preparation;

R.M. contributed to the assembly of the physical model and to tank testing; T.B. was co-investigator for the project and contributed to specification of tank test programme and to manuscript review.

Acknowledgments

This work was supported by the UK Engineering and Physical Sciences Research Council via the Marine Challenge grant EP/J010235/1 (X-MED). The authors would like to thank the IFREMER team of Boulogne-sur-Mer (France) for their help with the testing of the model, for granting access to some of their flow characterisation data used in this article and for the useful discussions during the data analysis phase of the project.

All the experimental measurements presented in this article can be accessed from http://dx.doi.org/10.7488/ds/2338 .

References

Ahmed, U., Apsley, D., Afgan, I., Stallard, T. and Stansby, P. (2017), 'Fluctuating Loads on a Tidal Turbine Due to Velocity Shear and Turbulence: Comparison of CFD with Field Data', *Renewable Energy* **112**, 235–246.

Bahaj, A., Batten, W. and McCann, G. (2007), 'Experimental verifications of numerical predictions for the hydrodynamic performance of horizontal axis marine current turbines', *Renewable Energy* **32**(15), 2479–2490.

Bahaj, A., Molland, A., Chaplin, J. and Batten, W. (2007), 'Power and thrust measurements of marine current turbines under various hydrodynamic flow

conditions in a cavitation tunnel and a towing tank', *Renewable Energy* **32**(3), 407–426.

Bearman, P. W. (1969), 'On vortex shedding from a circular cylinder in the critical Reynolds number regime', *J . Fluid Mech* **37**(3), 577–585.

Blackmore, T., Myers, L. E. and Bahaj, A. S. (2016), 'Effects of turbulence on tidal turbines: Implications to performance, blade loads, and condition monitoring', *International Journal of Marine Energy* **14**, 1–26.
URL: *http://www.sciencedirect.com/science/article/pii/S2214166916300297*

Chamorro, L. P., Hill, C., Morton, S., Ellis, C., Arndt, R. E. a. and Sotiropoulos, F. (2013), 'On the interaction between a turbulent open channel flow and an axial-flow turbine', *Journal of Fluid Mechanics* **716**, 658–670.

de Jesus Henriques, T., Tedds, S., Botsari, A., Najafian, G., Hedges, T., Sutcliffe, C., Owen, I. and Poole, R. (2014), 'The effects of wave-current interaction on the performance of a model horizontal axis tidal turbine', *International Journal of Marine Energy* **8**, 17–35.

Doman, D. a., Murray, R. E., Pegg, M. J., Gracie, K., Johnstone, C. M. and Nevalainen, T. (2015), 'Tow-tank testing of a 1/20th scale horizontal axis tidal turbine with uncertainty analysis', *International Journal of Marine Energy* **11**, 105–119.
URL: *http://linkinghub.elsevier.com/retrieve/pii/S2214166915000259*

Durán Medina, O., Schmitt, F., Calif, R., Germain, G. and Gaurier, B. (2015), Correlation between synchronised power and flow measurements , a way to characterize turbulence effects on a marine current turbine, *in*

'Proceedings of the 11th European Wave and Tidal Energy Conference', Nantes, France.

Durán Medina, O., Schmitt, F. G., Calif, R., Germain, G. and Gaurier, B. (2017), 'Turbulence analysis and multiscale correlations between synchronized flow velocity and marine turbine power production', *Renewable Energy* **112**, 314–327.

Fernandez-Rodriguez, E., Stallard, T. and Stansby, P. (2014), 'Experimental study of extreme thrust on a tidal stream rotor due to turbulent flow and with opposing waves', *Journal of Fluids and Structures* **51**(December 2015), 354–361.

Galloway, P. W., Myers, L. E. and Bahaj, A. S. (2014), 'Quantifying wave and yaw effects on a scale tidal stream turbine', *Renewable Energy* **63**, 297–307.

Gaurier, B., Davies, P., Deuff, A. and Germain, G. (2013), 'Flume tank characterization of marine current turbine blade behaviour under current and wave loading', *Renewable Energy* **59**, 1–12.

Gaurier, B., Germain, G., Facq, J., Johnstone, C., Grant, A., a.H. Day, Nixon, E., Di Felice, F. and Costanzo, M. (2015), 'Tidal Energy "Round Robin" Tests Comparisons between towing tank and circulating tank results', *International Journal of Marine Energy* **12**(2015), 87–109.

Germain, G. (2008), Marine current energy converter tank testing practices, *in* '2^{nd} International Conference on Ocean Energy (ICOE 2008)', number October, Brest, France, pp. 2–7.
URL: *http://archimer.ifremer.fr/doc/00022/13366/*

Hansen, M. O. L. (2008), *Aerodynamics of Wind Turbines*, 2ˆ{nd} edn, Earthscan.

Kolekar, N. and Banerjee, A. (2015), 'Performance characterization and placement of a marine hydrokinetic turbine in a tidal channel under boundary proximity and blockage effects', *Applied Energy* **148**, 121–133.
URL: *http://www.sciencedirect.com/science/article/pii/S0306261915003360*

Lust, E. E., Luznik, L., Flack, K. A., Walker, J. M. and Van Benthem, M. C. (2013), 'The influence of surface gravity waves on marine current turbine performance', *International Journal of Marine Energy* **3-4**, 27–40.

Luznik, L., Flack, K. A., Lust, E. E. and Taylor, K. (2013), 'The effect of surface waves on the performance characteristics of a model tidal turbine', *Renewable Energy* **58**, 108–114.
URL: *http://dx.doi.org/10.1016/j.renene.2013.02.022*

Martinez, R., Payne, G. S. and Bruce, T. (2017), Preliminary results on the effects of oblique current and waves on the loadings and performance of tidal turbines, *in* 'Proceedings of the 12^{th} European Wave and Tidal Energy Conference 2017', Cork, Ireland.

Mason-Jones, A., O'Doherty, D. M., Morris, C. E. and O'Doherty, T. (2013), 'Influence of a velocity profile & support structure on tidal stream turbine performance', *Renewable Energy* **52**, 23–30.

Mason-Jones, A., O'Doherty, D. M., Morris, C. E., O'Doherty, T., Byrne, C. B., Prickett, P. W., Grosvenor, R. I., Owen, I., Tedds, S. and Poole, R. J. (2012), 'Non-dimensional scaling of tidal stream turbines', *Energy*

44(1), 820–829.
URL: *http://dx.doi.org/10.1016/j.energy.2012.05.010*

MayGen Ltd. (2016), MeyGen Tidal Energy Project Phase 1. Project Environmental Monitoring Programme, Technical Report, Technical Report MEY-1A-70-HSE-018-I-PEMP.

McNaughton, J. (2013), 'Turbulence modelling in the near field of an axial flow turbine using code saturne'.

McTavish, S., Feszty, D. and Nitzche, F. (2014), 'An experimental and computational assessment of blockage effects on wind turbine wake development', *Wind Energy* **17**, 1515–1529.
URL: *http://onlinelibrary.wiley.com/doi/10.1002/we.1648/full*

Milne, I. A., Day, A. H., Sharma, R. N. and Flay, R. G. (2016), 'The characterisation of the hydrodynamic loads on tidal turbines due to turbulence', *Renewable and Sustainable Energy Reviews* **56**, 851–864.
URL: *http://dx.doi.org/10.1016/j.rser.2015.11.095*

Milne, I., Day, A., Sharma, R. and Flay, R. (2013), 'Blade loads on tidal turbines in planar oscillatory flow', *Ocean Engineering* **60**, 163–174.
URL: *http://linkinghub.elsevier.com/retrieve/pii/S0029801812004465*

Moriarty, P. J. and Hansen, A. C. (2005), AeroDyn Theory Manual, Technical Report NREL/TP-500-36881, National Renewable Energy Laboratory.
URL: *http://www.nrel.gov/docs/fy05osti/36881.pdf*

Mycek, P., Gaurier, B., Germain, G., Pinon, G. and Rivoalen, E. (2014), 'Experimental study of the turbulence intensity effects on marine current

turbines behaviour. Part I: One single turbine', *Renewable Energy* **66**, 729–746.

Parkinson, S. G. and Collier, W. J. (2016), 'Model validation of hydrodynamic loads and performance of a full-scale tidal turbine using Tidal Bladed', *International Journal of Marine Energy* **16**, 279–297.

Payne, G. S., Stallard, T. and Martinez, R. (2017), 'Design and manufacture of a bed supported tidal turbine model for blade and shaft load measurement in turbulent flow and waves', *Renewable Energy* **107**, 312–326.

Payne, G. S., Stallard, T., Mullings, H. R. and Martinez, R. (2017), Experimental Investigation into Unsteady Loads on Horizontal Axis Tidal Turbines, *in* '12^{th} European Wave and Tidal Energy Conference', Cork, Ireland.

Schepers, J. G., Boorsma, K., Gomez-Iradi, S., Schaffarczyk, P., Madsen, H. A., Sørensen, N. N., Shen, W. Z., Lutz, T., Schulz, C., Herraez, I. and Schreck, S. (2014), Final report of IEA Task 29: Mexnext (Phase 2), Technical Report ECN-E–14-060, Energieonderzoek Centrum Nederland (ECN).
URL: *https://www.ecn.nl/publications/PdfFetch.aspx?nr=ECN-E–14-060*

Smilden, E., Sørensen, A. and Eliassen, L. (2016), 'Wind Model for Simulation of Thrust Variations on a Wind Turbine', *Energy Procedia* **94**(1876), 306–318.
URL: *http://dx.doi.org/10.1016/j.egypro.2016.09.188*

Stallard, T., Feng, T. and Stansby, P. (2015), 'Experimental study of the mean wake of a tidal stream rotor in a shallow turbulent flow', *Journal of Fluids and Structures* **54**, 235–246.

Storey, R. C., Cater, J. E. and Norris, S. E. (2016), 'Large eddy simulation of turbine loading and performance in a wind farm', *Renewable Energy* **95**, 31–42.
URL: *http://dx.doi.org/10.1016/j.renene.2016.03.067*

Thé, J. and Yu, H. (2017), 'A critical review on the simulations of wind turbine aerodynamics focusing on hybrid RANS-LES methods', *Energy* **138**, 257–289.

Thorpe, S. (2007), *An Introduction to Ocean Turbulence*, Cambridge University Press.